Am J Nucl Med Mol Imaging 2013;3(4):336-349
www.ajnmmi.us /ISSN:2160-8407/ajnmmi1303004

Original Article

In vivo validation and 3D visualization of broadband ultrasound molecular imaging

Xiaowen Hu[1*], Charles F Caskey[1*], Lisa M Mahakian[1], Dustin E Kruse[1], Julie R Beegle[1], Anne-Emilie Declèves[2], Joshua J Rychak[3], Patrick L Sutcliffe[1], Kumar Sharma[2], Katherine W Ferrara[1]

[1]Department of Biomedical Engineering, University of California, Davis, One Shields Ave, Davis, CA 95616, USA; [2]Center for Renal Translational Medicine, Division of Nephrology-Hypertension, Department of Medicine, University of California, San Diego, La Jolla, CA 92093, USA; [3]Targeson Inc., 3550 General Atomics Court, MS 02-444, San Diego, CA 92121, USA. [*]These authors contributed equally to this manuscript.

Received March 7, 2013; Accepted April 11, 2013; Epub July 10, 2013; Published July 15, 2013

Abstract: Ultrasound can selectively and specifically visualize upregulated vascular receptors through the detection of bound microbubbles. However, most current ultrasound molecular imaging methods incur delays that result in longer acquisition times and reduced frame rates. These delays occur for two main reasons: 1) multi-pulse imaging techniques are used to differentiate microbubbles from tissue and 2) acquisition occurs after free bubble clearance (>6 minutes) in order to differentiate bound from freely circulating microbubbles. In this paper, we validate tumor imaging with a broadband single pulse molecular imaging method that is faster than the multi-pulse methods typically implemented on commercial scanners. We also combine the single pulse method with interframe filtering to selectively image targeted microbubbles without waiting for unbound bubble clearance, thereby reducing acquisition time from 10 to 2 minutes. The single pulse imaging method leverages non-linear bubble behavior by transmitting at low and receiving at high frequencies (TLRH). We implemented TLRH imaging and visualized the accumulation of intravenously administrated integrin-targeted microbubbles in a phantom and a Met-1 mouse tumor model. We found that the TLRH contrast imaging has a ~2-fold resolution improvement over standard contrast pulse sequencing (CPS) imaging. By using interframe filtering, the tumor contrast was 24.8±1.6 dB higher after the injection of integrin-targeted microbubbles than non-targeted control MBs, while echoes from regions lacking the target integrin were suppressed by 26.2±2.1 dB as compared with tumor echoes. Since real-time three-dimensional (3D) molecular imaging provides a more comprehensive view of receptor distribution, we generated 3D images of tumors to estimate their volume, and these measurements correlated well with expected tumor sizes. We conclude that TLRH combined with interframe filtering is a feasible method for 3D targeted ultrasound imaging that is faster than current multi-pulse strategies.

Keywords: Targeted microbubbles, ultrasound molecular imaging, angiogenesis, 3D visualization

Introduction

Ultrasound contrast agents (microbubbles) are gas-filled particles that range in diameter from hundreds of nanometers to several microns. Microbubbles oscillate in response to ultrasound excitation and produce nonlinear echoes under suitable conditions [1]. Because tissue generates echoes that are more linear than microbubbles, strong nonlinear echoes from microbubbles can be used to selectively detect circulating microbubbles while suppressing echoes from tissue. Multiple contrast imaging techniques have been developed, including harmonic and multi-pulse imaging [2]. In harmonic imaging, a long acoustic pulse is emitted that causes microbubbles to generate nonlinear echoes. This method results in a high contrast to tissue ratio but the long acoustic pulse degrades axial resolution [3, 4]. Multi-pulse imaging strategies, such as pulse inversion imaging and contrast pulse sequencing (CPS), are commonly implemented on clinical ultrasound scanners and are based on the transmission of multiple pulses with varied amplitudes and phases [5, 6]. A linear algebraic combination of the resultant echoes (for example: summation and subtraction) emphasizes memory nonlinearities in the microbubble response compared to memoryless nonlinearities in the tissue response. CPS imaging provides high sensitivity, allowing for the detection of microbubble echoes with a low-mechanical index (MI) acoustic field (<0.1) [6-8]. However, transmitting multiple pulses along each ultrasound scan line reduces the imaging frame rate, which introduces limitations with regard to 3D or 4D ultrasound imaging.

The transmission-at-low reception-at-high (TLRH) contrast imaging technique overcomes these limitations by driving bubbles with a short low frequency pulse, causing the microbubble to generate echoes across many frequencies (ie. a broadband echo) [9]. The broadband echo is received by a high frequency transducer, resulting in a high contrast-to-tissue ratio and spatial resolution. We have previously implemented TLRH on a Siemens Antares system (T1.5R5.5, where 1.5 and 5.5 MHz are the center frequencies of the transducer elements used for transmission and reception) and others have done the same using VisualSonics Vevo 770 system (T2R30) [10, 11].

Due to their micron-scale diameter, microbubbles circulate solely in the vascular compartment. Conjugation of ligands to microbubble lipid shells through a covalent coupling method allows intravenously-administered microbubbles to specifically bind to upregulated receptors on diseased vascular endothelium [12]. Various targeting ligands have been used to detect receptors related to inflammation and angiogenesis [13-20]. In particular, cyclic RGD (cRGD) peptides have been used as targeting ligands in several studies to image $\alpha_v\beta_3$ on angiogenic tumor vasculature, and we use these bubbles here to target Met-1 breast cancer tumors in mice [21-23].

A challenge for ultrasound imaging of targeted microbubbles is the differentiation of bound and circulating microbubbles in a short period of time. Since circulating microbubbles clear from the target volume faster than bound microbubbles, a common imaging strategy is to acquire bound microbubble echoes 7-15 minutes after injection when freely circulating microbubbles have cleared from the blood pool [24-29]. The procedure is time-consuming, making clinical translation difficult, and can lead to an underestimation of bound microbubble echoes due to the destruction of bound microbubbles during the waiting time. Furthermore, the time point to assess bound microbubbles is difficult to estimate because the persistence time of unbound circulating microbubbles varies with microbubble formulations and experimental settings from 2 minutes to 10 minutes [18, 30]. Therefore, a fast ultrasound molecular imaging method is desirable for both pre-clinical and clinical applications.

In this study, we suppress echoes from circulating bubbles while retaining those from targeted bubbles by filtering sequential frames of images with flowing and stationary microbubbles. Interframe filters have been used to differentiate bound and circulating microbubbles *in vitro*; here we apply this method for *in vivo* imaging [10, 31].

Three-dimensional (3D) ultrasound visualization of targeted microbubbles provides a comprehensive view of receptor distribution, allowing for precise guidance of therapeutic interventions by surveying the diseased region in real time to guide ablation or biopsy. Therefore, our overall goal is to create a fast acquisition strategy for 3D molecular imaging. In this work, CPS imaging was used as a standard low power and non-destructive multi-pulse imaging technique for comparison. The resolution of a single pulse broadband imaging scheme, T2R15 (with 2.25 MHz transmission and 15 MHz reception), was compared with 2.25 MHz multi-pulse (CPS) imaging *in vitro* using the same transducers and instrumentation. Broadband T1R5.5 (transmission at 1.5 MHz and reception at 5.5 MHz) with interframe filtering was applied to visualize cRGD microbubble accumulation in the vasculature of a murine breast tumor model and compared to images produced by 7 MHz multi-pulse (CPS) imaging with a 7 minute waiting period. 3D targeted images were acquired and linear regression analysis was used to relate the detected 3D volume to the tumor weight. This work demonstrates feasibility of using ultrasound and targeted microbubbles for high-resolution, fast molecular imaging in 3D.

Material and methods

Laboratory equipment, consisting of single element transducers, pulsers and receivers were used within the *in vitro* studies to provide a direct comparison of broadband (TLRH) and multi-pulse (CPS) imaging. *In vivo* studies were conducted using the Siemens Sequoia for multi-pulse imaging (due to the superior CPS performance) while broadband TLRH images were acquired on the Siemens Antares due to the availability of a custom array.

Microbubble preparation

Four types of microbubbles were used. Non-biotinylated and biotinylated microbubbles used for *in vitro* studies were produced in our laboratory with a concentration of 2×10^9 particles/ml and a mean diameter of 2.0±0.5 μm [32]. The combination of 1,2-distearoyl-sn-glycero-3-phosphatidylcholine (DSPC) and 1,2-distearoyl-sn-glycero-3-phosphoethanolamine-N-[methoxy (polyethyleneglycol)-2000] (DSPE-PEG2k) (molar ratio = 90:10) and perfluorobutane resulted in non-biotinylated bubbles; DSPC: DSPE-PEG2k: and DSPE-PEG2k-Biotin (molar ratio = 90:5:5) were combined to produce biotinylated microbubbles. These microbubbles were diluted in PBS in order to acquire echoes from individual microbubbles. To target murine tumor vasculature *in vivo*, Visistar-Integrin® cyclic-RGD bearing microbubbles (cRGD microbubbles, Targeson Inc., San Diego, CA; DSPE-PEG-PDP, PEG-40, and Perfluorobutane) with a median diameter of 2.5±0.1 μm and concentration of approximately 1×10^9 microbubbles/ml were used. cRGD microbubbles exhibit affinity to upregulated $\alpha_v\beta_3$ integrins expressed in angiogenic tumor vasculature [21]. Targestar® non-targeting microbubbles (Targeson Inc., San Diego, CA) were also employed in this study as a comparison to cRGD targeting. Based on our experience, the peak intensity of both cRGD and non-targeted microbubble echoes in the mouse Met-1 tumor region occurred in less than 2 minutes after tail vein injection and both were cleared from the blood stream after ~7 minutes.

In vitro experiments

In vitro, the multi-pulse CPS sequence consisted of an inverted 2.25 MHz pulse with full amplitude and two non-inverted 2.25 MHz pulses with half amplitude prior to and after the inverted pulse (-0.5, 1, -0.5 sequence) [33]. The input 2.25 MHz pulses were experimentally measured from the output of a 2.25 MHz focused broadband single-element transducer driven by a single-cycle sine wave. For broadband TLRH imaging *in vitro*, the transmitted pulse was identical to the inverted pulse used in the CPS sequence.

The CPS pulses and T2R15 pulse were programmed on an arbitrary waveform generator (AWG 2021, Sony/Tektronix, Japan), amplified by a linear RF power amplifier (325LA; ENI, Rochester, NY) and were used to drive the 2.25 MHz transducer (model V3966; Olympus-NDT, Waltham, MA). The CPS sequence was optimized to minimize both the fundamental and second harmonic energy backscattered from a rigid linear target [33]. In the center of this V3966 transducer, either a 2.25 MHz single element transducer (V323SM, Olympus-NDT, Waltham, MA) or a 15 MHz single element transducer (V313SM, Olympus-NDT, Waltham, MA) was placed to receive echoes. The combination of 2.25 MHz transmission and 2.25 MHz reception was used for CPS imaging, while the combination of 2.25 MHz transmission and 15 MHz reception was used for T2R15 imaging. The peak negative pressure studied here ranged from 100 kPa to 500 kPa and was calibrated by a needle hydrophone (Onda, Sunnyvale, California). In order to assess the sensitivity of detecting single circulating microbubble echoes in both imaging modes, a dilute microbubble dispersion (a dilution factor of 1×10^5) was infused using a syringe pump (Harvard Apparatus, Holliston, MA) through a 200 μm inner diameter cellulose tube (Spectrum Laboratories, Inc., Rancho Dominguez, CA) with a flow rate of 5 mm/s. Received echoes were pre-amplified (BR-640A, Ritec Inc., Warwick, RI), digitized by a MATLAB (MathWork, Natick, MA) controlled DPO4034 oscilloscope (Tektronix, Beaverton, OR), and processed off-line. To assess the sensitivity of detecting a single bound microbubble, a cellulose tube was coated with Neutravidin (Sigma-Aldrich, St. Louis, MO) and echoes from bound biotinylated microbubbles were analyzed. In order to evaluate the imaging resolution, microbubbles (10^8 particles/ml) were pumped through two cellulose tubes separated by 400 μm and were imaged by TLRH and CPS modes. Both TLRH and CPS M-mode images consisted of 512 scan lines and had a 40 dB dynamic range. The -6 dB width of visualized circulating microbubbles was measured to represent the spatial resolution in the axial direction.

Table 1. Experimental sample size

	N
1. TLRH and interframe FIR filter (Figures 3 and 4)	5
2. Image intensity of TLRH with interframe filtering at various time points (Figure 5)	3
3. Image comparison between TLRH image with interframe FIR filtering and CPS (Figure 6)	3
4. Tumor volume measurements from 3D TLRH imaging with interframe filtering (Figure 8)	16
5. The comparison of 3D tumor volume measurements between TLRH with interframe filtering and CPS imaging (Figure 8)	3
6. 3D visualization of CPS and TLRH images (Figure 7)	3

Mouse model

All animal studies were conducted under a protocol approved by the Institutional Animal Care and Use Committee of the University of California, Davis. Female FVB mice (6-7 weeks, 25-30 g, Charles River, MA) carrying highly metastatic Met-1 tumors in their 4th mammary fatpad were scanned during this study [34]. The syngeneic Met-1 tumor has an epithelial phenotype with significant angiogenesis demonstrated by CD31-expressing blood vessels. We have previously acquired confocal microscopy images of the vasculature in tumors from DiI-cRGD-MB-treated animals which demonstrate the accumulation of targeted MB within the vasculature [21]. Scanned Met-1 tumors had a mean diameter of 5 mm. Before ultrasound scanning, the scanned region was shaved and further treated with depilatory (Veet; Reckitt Benckiser, Parsippany, NJ). Throughout imaging, mice were anesthetized with 2% isoflurane (Halocarbon Laboratory, River Edge, NJ) in oxygen (2 L/min) and positioned on the scanning stage with the tumor region immersed in a 37°C water bath to maintain body temperature. For each scan, 50 μl of the microbubble dispersion was administrated intravenously via tail vein injection (bolus injection). If multiple injections were employed, a 30-minute interval between injections was used to minimize the effect of the previous injection. A total number of 28 mice were scanned in this study, as summarized in **Table 1**. An initial group size of n=5 was selected in the comparison of the image intensity with targeted and non-targeted agents based on an alpha of 0.05, standard deviation of 20%, difference in image mean of 40% and power of 0.8. We found that the difference between the targeted and control agents was larger (>than 60%) and therefore reduced study groups sizes to n=3.

Immunofluorescence

In order to verify the presence of the expression of $\alpha_v\beta_3$ on the tumor vasculature, immunofluorescence images were obtained. Met-1 tumors were excised immediately after imaging, frozen in OCT compound (Miles Laboratories, Naperville, IN), and cryosectioned at 5 μm thickness. Frozen tumor sections were fixed in 4% paraformaldehyde, permeabilized with 0.1% Triton X-100, and blocked in PBS containing 10% newborn calf serum, 1% BSA, and 0.02% Triton X-100. The integrin β_3 and the endothelial cells were visualized with the antisera using a rabbit anti-CD61 antibody (Millipore, Billerica, MA) and a rat anti-CD31 antibody (AbDSerotec, Raleigh, NC), respectively. Secondary antibodies included AlexaFluor 594-conjugated anti-rabbit and AlexaFluor 488-conjugated anti-rat antibodies (Invitrogen, Carlsbad, California). DAPI (ProLong Gold; Invitrogen, Carlsbad, California) staining was performed to insure that a similar number of cells was present in the field of view. Immunofluorescence was observed with a confocal LSM 510 microscope (Zeiss, Germany) and representative photographic images were acquired at a magnification of 63x.

In vivo CPS imaging

CPS imaging was implemented on a Sequoia® 512 system (Siemens, Issaquah, WA) with a 15L8 transducer operating at a center frequency of 7 MHz. The transmitted acoustic power in CPS (0.09 MI, approximately 230 kPa peak negative pressure), the CPS gain (-12 dB), linear TGC curve, and other acoustic parameters were optimized and kept constant throughout this study. The procedure using CPS to visualize bound microbubbles was described in our previous work [21]. Briefly, CPS images were

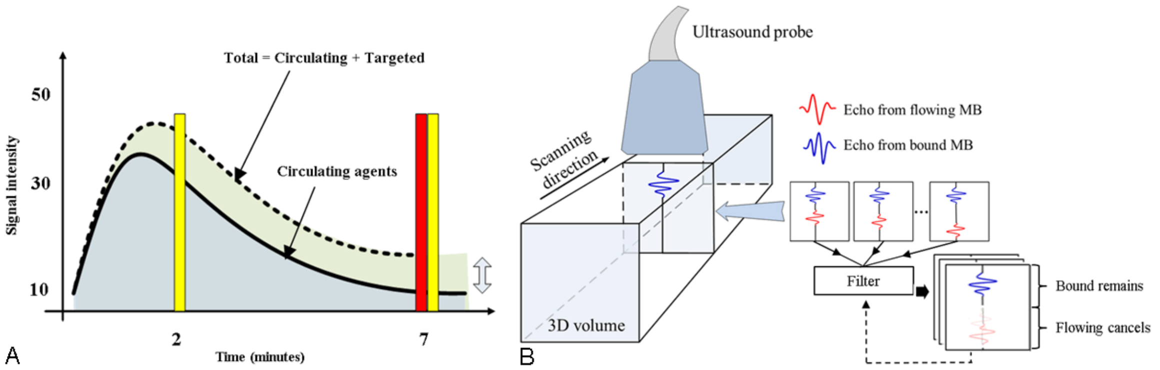

Figure 1. Time points for imaging during bubble circulation and interframe filtered volumetric imaging. A: Broadband (T1R5.5) RF data (yellow bar) were acquired at 2 minutes (when both circulating microbubbles and bound microbubbles were present in the blood stream) and 7 minutes (primarily bound microbubbles) after targeted microbubble injection. Multi-pulse (CPS) image data were acquired 7 minutes after the injection of microbubbles (red bar); thus, most circulating microbubbles had cleared from the vasculature while bound microbubbles were retained. B: Multiple image frames were acquired in each plane and then algebraically combined and filtered to differentiate selectively image bound microbubbles. The ultrasound probe was then scanned in the third dimension to capture a volumetric data set.

Table 2. Acoustic parameters

	CPS *in vitro*	TLRH *in vitro*	CPS *in vivo*	TLRH *in vivo*
Frequency (Transmission/Reception) (MHz)	2.25/2.25	2.25/15	7/7	1.5/5.5
Peak Negative Pressure (kPa)	100-500	100-500	230	230

acquired 7 minutes after the initial injection of cRGD microbubbles to allow for the clearance of freely circulating microbubbles (**Figure 1A**, red bar). CPS images acquired at this time were compared with images produced by T1R5.5 that were acquired 2 and 7 minutes after the microbubble injection and with interframe filtering. The region of accumulated microbubbles was defined as the region in which the video intensity was above 15% of the system maximum value. To generate a 3D image data set, a CPS image was acquired on each imaging plane across the tumor region (5 mm) with a ~0.7 mm step to advance the transducer. Seventy frames of averaged CPS images were reconstructed by MATLAB and visualized by ImageJ 3D Viewer (NIH).

In vivo TLRH imaging, interframe filtering

The T1R5.5 imaging mode was implemented on an Antares® system (Siemens, Issaquah, WA) with a customized co-linear transducer [35]. The transducer's two low frequency outer arrays were excited simultaneously to form a single cycle 1.5 MHz pulse. The center 5.5 MHz array received high frequency echoes from microbubbles. The transmitted peak negative pressure was 230 kPa with a 10 Hz frame rate and a linear TGC curve. In **Table 2**, acoustic parameters for both *in vitro* and *in vivo* studies are summarized. Thirty frames of radiofrequency (RF) data were digitized and acquired at 2 and 7 minutes after the injection of microbubbles (**Figure 1A**, yellow bar). Acquired RF data were processed in two steps. First, for the return from each received pulse, microbubble echoes were separated from tissue echoes by a band-pass filter with a pass-band from 5.5 MHz to 15 MHz. Second, an interframe filter was applied to identical pixels in multiple image frames in order to separate bound microbubble from circulating microbubble echoes. The interframe filter was either an averaging filter (no memory, thus all frames are averaged equally) or a 7th order infinite impulse response (IIR) elliptic filter (a filter than retains the memory of each output and therefore each output is based on previous inputs and outputs) [10]. The elliptic filter had a stop-band at 0.2 Hz, 50 dB ripple suppression in the transient band and step initialization. The averaging filter is a low-pass filter, with a cut-off frequency of 0.2 Hz and with

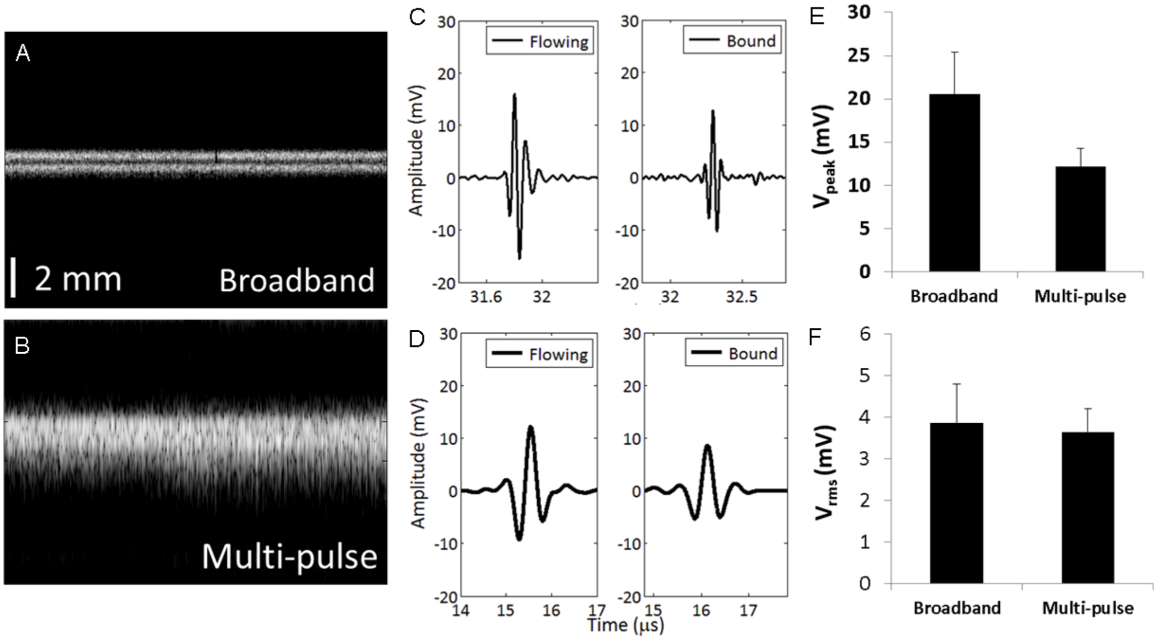

Figure 2. Broadband imaging achieves higher resolution than multi-pulse imaging in less time with equal sensitivity. Comparative performance of broadband (T2R15) and multi-pulse (CPS) imaging *in vitro*. A, B: Microbubbles flowing through two 200 μm-diameter tubes, separated by 400 μm, were imaged by (A) broadband (T2R15) imaging and (B) multi-pulse (CPS) imaging mode. Both images have a 40-dB dynamic range and consist of 512 scan lines. The vertical scale bar in (A) and (B) represents 2 mm. C: Broadband (T2R15) echo from a single circulating (left) and bound microbubble (right). D: Multi-pulse signals (CPS, post-summation) from a single circulating (left) and bound (right) microbubble. E: For echoes received from the same bound microbubble, the echo amplitude was greater for broadband excitation and (F) the root mean squared integral of the echo amplitude received from a single microbubble by the 15 MHz and 2.25 MHz transducers was similar. The transmitted pressure was 250 kPa for (C-F).

uniform coefficients. Step initialization of the IIR filter was chosen based on a previous study [10]. The interframe filter was also applied to the detected video-intensity data acquired 2 minutes after the injection of microbubbles to evaluate flowing microbubble echo cancellation with RF, as compared with detected, data.

In order to verify the specificity of the detection of bound microbubbles by interframe filtered TLRH imaging, cRGD and non-targeted microbubbles were injected separately and their accumulation in the tumor region was visualized by both CPS and TLRH imaging. Furthermore, TLRH images that were acquired 2 minutes after microbubble injection and processed by the interframe filters were compared to TLRH images acquired after 7 minutes. For TLRH images, mean contrast intensities over manually selected tumor regions were calculated. The difference between mean intensities measured in 2 minutes and 7 minutes was tested for significance (Wilcoxon rank sum test, $p<0.05$ indicates significance). We also evaluated each imaging technique based on the log of the ratio of the image intensity within the tumor (I_{tumor}) to the image intensity in healthy tissue (I_{tissue}). Therefore, the gain in decibels (G_{dB}) was computed by $G_{dB} = 20\log_{10}(\frac{I_{tumor}}{I_{tissue}})$. The tumor-to-tissue ratio measures the ability to selectively image bound microbubbles while successfully suppressing echoes from tissue.

Three-dimensional imaging

The 3D scanning system described previously-consists of a heated water bath with a polymethylpentene (TPX) sheet covered base (0.5 mm), a small animal holder controlled by a mechanical three axis positioning stage (Edmund Optics, Barrington, NJ), a nose cone used to deliver anesthesia, a linear actuator (PQ12; Firgelli Technologies, Canada) to move the transducer cross the scanning region and an electromagnetic spatial measurement system (Aurora; Northern Digital Inc., Canada) to track the position of the ultrasound transducer through an attached 6-degree-of-freedom sen-

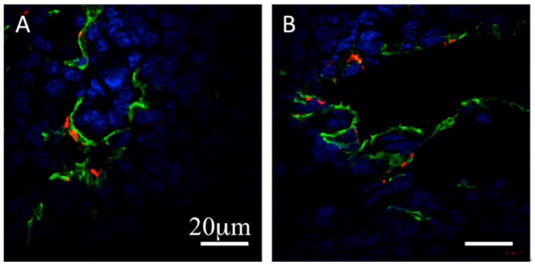

Figure 3. A, B: Representative confocal fluorescent images of the tumor endothelium (anti-CD31 staining, green), β_3-integrin (anti-CD61 staining, red), and nuclei (DAPI, blue). The expression of β_3-integrin was co-localized with tumor endothelium. The scale bar is 20 µm.

sor [36]. The electromagnetic measurement system was calibrated using a single point technique [36, 37]. The transducer is mounted underneath the water bath bottom, facing the scanning region against the TPX sheet. Ultrasound gel (Aquasonic, Fairfield, NJ) was used as a coupling agent between the transducer surface and the TPX sheet. A PC running Linux communicates and controls the linear actuator through a USB port (minimum step of ~200 µm and maximum speed of 5 mm/s) and the tracking system via a serial port with a 3D accuracy of ~600 µm.

3D visualization of TLRH imaging was similar to 3D CPS with each voxel representing interframe filtered data (**Figure 1B**). The tumor volume was estimated from bound microbubble images by manually choosing regions of accumulation in each imaging plane, multiplying the area with distance between two imaging planes, and then summing products together. In order to demonstrate that the volume delineated by bound microbubbles represented the tumor region, tumors (n=16) were excised after scanning and weighed to compare the tumor volume measured from 3D images (linear regression, $R^2>0.8$ indicates significant correlation).

Results

In this section, we first validate TLRH imaging *in vitro* as a method that can detect microbubble echoes with superior performance compared to the widely used CPS imaging technique, while increasing acquisition speed by eliminating the need for multiple pulses. Expression of the $\alpha_v\beta_3$ integrin, which was the vascular target in this study, is then verified by immunohistochemical-staining. *In vivo* molecular imaging using TLRH imaging with the addition of interframe filtering is then validated, and feasibility of fast 3D visualization of the tumor volume is shown.

In vitro studies

As demonstrated in previous studies, broadband TLRH imaging improved spatial resolution as compared with a single frequency strategy; here, we directly compare transmission at 2 MHz and reception at 15 MHz with multi-pulse (CPS) imaging. Two cellulose tubes containing circulating microbubbles were resolved in the TLRH M-mode image (**Figure 2A**) but not in the CPS image (**Figure 2B**). The full-width at half maximum (FWHM) of a single tube in the TLRH image was 0.48 mm compared to 0.95 mm in the CPS image, indicating that TLRH imaging was capable of resolving closely spaced targets. The background echoes from the cellulose tube were cancelled (~28 dB) either by high frequency reception in the TLRH imaging mode or by the linear combination of pulses received following the transmission of a CPS sequence.

The echoes received from a single circulating or bound bubble using TLRH were then compared to the algebraic output from the summed CPS pulses to demonstrate the comparative performance of TLRH imaging (**Figure 2C** and **2D**). The TLRH echo from single microbubbles had a higher center frequency and wider spectrum than that from bound microbubbles; however the root mean square of the TLRH signals did not differ significantly from the algebraic sum of CPS imaging (**Figure 2F**). In particular, echoes from identical microbubbles (as in **Figure 2C** and **2D** for bound bubbles) differed in frequency content and those obtained with broadband imaging had a greater peak amplitude and similar root mean squared intensity to multi-pulse imaging.

Immunohistochemistry verifies the expression of the target integrin on tumor vasculature

Immunofluorescence staining of the Met-1 tumor with both anti-CD31 and anti-CD61 antibodies demonstrated that the β_3-integrins were expressed and co-localized with the endothelium visualized by CD31 staining (**Figure 3A**, **3B**).

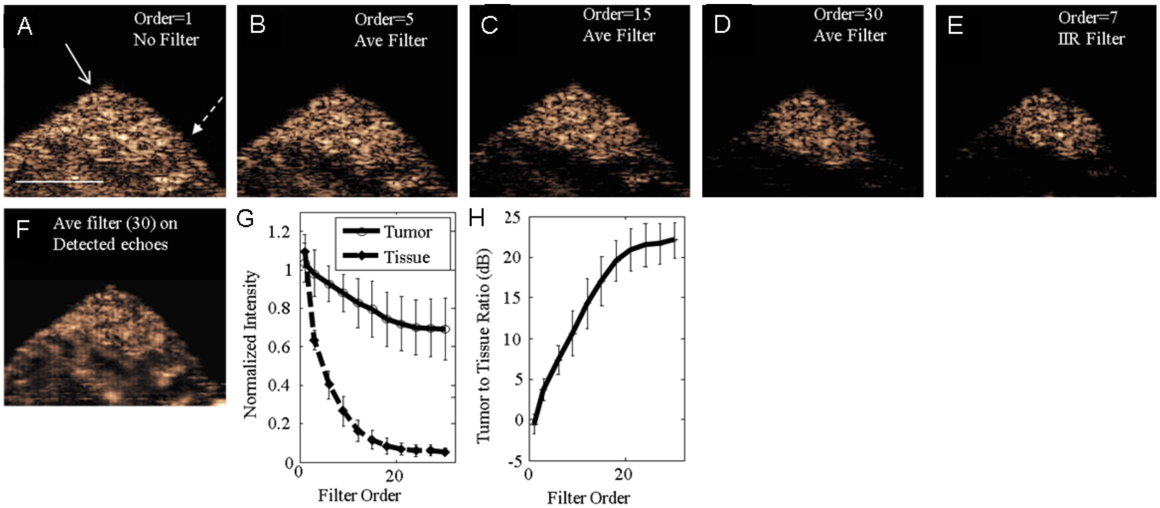

Figure 4. Selectively imaging bound microbubbles 2 minutes after injection by applying interframe filters on RF (A-E) and detected (F) data. A: The broadband (T1R5.5) image without interframe filtering contains echoes from both bound and circulating microbubbles. Solid arrow indicates the tumor region and dashed arrow indicates the surrounding tissue. B-D: Increasing the averaging (Ave) filter order (ie. the number of images averaged), the circulating microbubble echoes in the surrounding tissue region are gradually suppressed, while bound microbubble echoes in the tumor region are retained. E: The 7th order IIR filter achieves similar performance as the 30th order averaging filter but with a lower filter order. F: A 30th order averaging filter is applied to detected microbubble echoes. G: With filtering, the mean normalized intensity in the tumor region decreased by a smaller amount compared with the surrounding tissue. H: The log ratio of contrast intensity in the tumor region, compared with surrounding tissue, reached a peak value of 22.1±2.2 dB with increasing interframe averaging filter order. Scale bar represents 5 mm. Error bars represent variations of bound microbubble contrast intensity in n=5 mice.

Interframe filtering selectively images bound targeted bubbles

We have previously demonstrated that averaging image frames reduces the image amplitude resulting from circulating, as compared with bound microbubbles, by filtering CPS images acquired at 7 minutes after injection [21]. To test whether bound microbubbles can be detected and differentiated in a tumor by TLRH imaging at two minutes after injection, an averaging interframe filter was applied to the TLRH RF data to suppress circulating microbubble echoes without decreasing the echoes from bound agents (here transmission at 1.5 MHz and reception at 5.5 MHz was chosen for in vivo imaging). By increasing the averaging filter order from 1 to 30 (where order 1 indicated the absence of a filter) echoes from circulating microbubbles were gradually diminished (**Figure 4A-D**). With an averaging filter order of 30, echoes from circulating microbubbles in the surrounding tissue were highly suppressed (26.2±2.1 dB, **Figure 4D**, **4G**), while the signal intensity within the tumor was reduced to approximately 80% of its original intensity, thus highlighting the tumor region with a tumor-to-tissue ratio of 22.1±2.2 dB (**Figure 4H**). The tumor-to-tissue ratio of 23.2±2.5 dB (n=5) achieved with a 7th order IIR filter (**Figure 4E**) was slightly greater than that obtained with the 30th order averaging interframe filter. After pixel-by-pixel subtraction of the IIR and averaging filtered images, the difference in intensity was ~12% of the filtered images. The IIR filter was therefore applied in the remaining *in vivo* studies. The application of the averaging or IIR (not shown) filter on detected image data (rather than RF data) was not sufficiently sensitive to eliminate echoes from regions with a high circulating microbubble concentration (**Figure 4F**), and therefore, the processing was applied to the RF images in all remaining studies.

As early as two minutes after microbubble injection, the filtered images demonstrate the difference between the concentrations of targeted and control microbubbles within the tumor. After interframe filtering at two minutes after injection, the mean contrast intensity in the tumor region resulting from the injection of cRGD-conjugated microbubbles (**Figure 5A**)

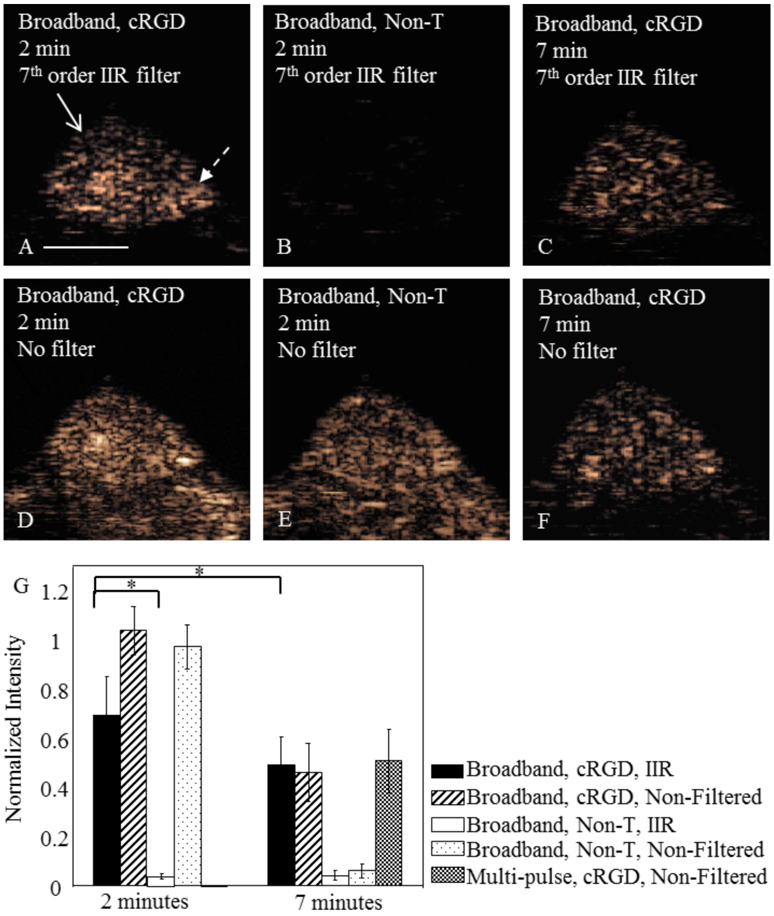

Figure 5. Comparison of filtered and non-filtered images obtained with targeted and control microbubbles in a mouse tumor model. A, D: Interframe filtered broadband (T1R5.5) images of cRGD microbubbles highlight the tumor region due to the retention of cRGD microbubbles (normalized intensity of 0.69±0.16) and suppression of flowing microbubble echoes. B, E: The injection of non-targeted microbubbles does not generate significant contrast intensity in the broadband (T1R5.5) image after interframe filtering (normalized intensity in the tumor region of 0.04±0.01). C, F: Interframe filtering applied to the data acquired 7 minutes after microbubble injection does not significantly alter the contrast intensity of bound microbubbles. A, F: Both images show the presence of bound cRGD microbubbles, but through different approaches. Image (A), bound microbubble echoes were acquired 2 minutes after the cRGD microbubble injection and were differentiated from circulating microbubble echoes by the 7th order IIR filter; while on image (F), image data were acquired 7 minutes after the microbubble injection when most circulating microbubbles were cleared from the blood stream. The scale bar represents 5 mm. The solid arrow indicates tumor region and dashed arrow indicates normal tissue region. G: Normalized intensity in the tumor region with varied scenarios (n=5, significance was achieved when $p<0.05$). The normalized intensity of bound cRGD microbubbles in the tumor region was visualized by multi-pulse (CPS) imaging at the 7 minute time point and compared to that with wideband imaging with interframe filtering.

was 24.8±1.6 dB higher than that resulting from non-targeted microbubbles (**Figure 5B**, **5G**). At the same time point, cRGD and non-targeted microbubbles generated similar contrast intensity on unfiltered TLRH images (**Figure 5D**, **5E**). Seven minutes after microbubble injection, filtered and unfiltered TLRH images of bound microbubbles (**Figure 5C**, **5F**) were of similar intensity (and thus the filter does not reduce the signal from the bound agent). Comparing the 2 and 7 minute filtered image of bound microbubbles, the mean intensity was 3.5±0.8 dB lower at 7 as compared with 2 minutes after injection, likely resulting from gradual loss of the targeted microbubbles from the vasculature (**Figure 5A**, **5G**). CPS multi-pulse imaging of RGD-targeted agents at 7 minutes after injection resulted in a similar image intensity as the single pulse broadband TLRH strategy (**Figure 5G**).

In the same tumor plane, filtered (7th order IIR filter) TLRH images of cRGD microbubbles and non-targeted microbubbles that were acquired at 2 minutes after injection (**Figure 6A**, **6B**) were morphologically similar to CPS targeted images acquired 7 minutes after the injection (**Figure 6C**, **6D**). While a minimal accumulation of non-targeted microbubbles was observed with either strategy, the difference in the area of accumulated cRGD microbubbles in the filtered T1R15 and CPS images was 14±3% (n=3), likely resulting from differences in the plane of acquisition between the two transducers and systems.

Time course of targeted bubble echoes

The loss of bound agents from the endothelium was then confirmed by acquiring images of

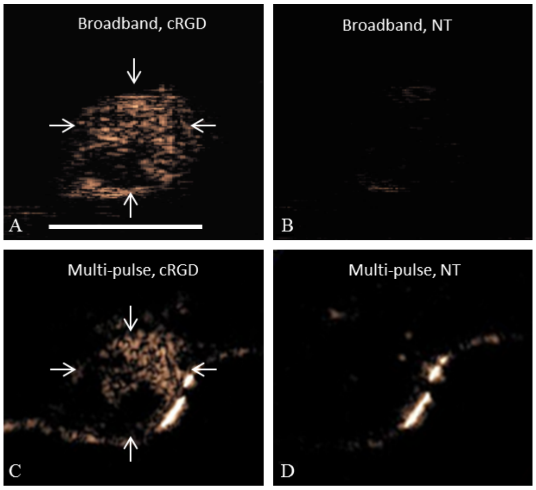

Figure 6. Broadband (T1R5.5) images and multi-pulse (CPS) images acquired in the same tumor plane. A, B: Interframe filtered broadband images acquired (A) 2 minutes after cRGD microbubble injection and (B) non-targeted microbubble injection. C, D: CPS images acquired 7 minutes after the injection of (C) cRGD and (D) non-targeted (NT) microbubbles. The scale bar represents 5 mm. Arrows indicate the tumor region. Comparison was performed in n=3 tumors.

bound agents at additional time points (**Figure 7**). The maximum bound microbubble intensity occurred between 2 and 5 minutes after injection (**Figure 7B**, **7F**) and slowly decreased over 8 minutes (**Figure 7E**, **7F**). The bound microbubble intensity measured at the 8 minute time point was decreased by 5.7±0.5 dB as compared to the 2 minute time point (n=3). Images acquired at 0.5 minutes after injection (**Figure 7A**) show that the tumor has not fully accumulated the targeted agent and the regions of circulating agent remain visible in the filtered images, likely due to the high volume of circulating agent.

3D acquisition and visualization of tumors

3D volumes of both CPS (**Figure 8A**) and TLRH (**Figure 8B**, **8C**) molecular images were then rendered to show the volume distribution of bound microbubbles. On both CPS and TLRH 3D volume images, the entire tumor volume contained the targeted agents, while the intensity of bound microbubbles in the surrounding tissue region was low. 3D tumor volume measurements of bound microbubbles were correlated (R^2=0.85) to tumor weight with a slope of ~1.2 mg/mm^3 (**Figure 8D**), slightly greater than the Met-1 tumor density of ~1.03 mg/mm^3. Two 3D volume images (**Figure 8E**, **8F**) representing the maximum and the minimum tumor volume studied are included as exemplary images. The volume measured using TLRH 3D imaging was similar to the measurement on CPS 3D imaging with a difference less than 15% (n=3).

Discussion

Ultrasound has a unique role to play in molecular imaging, given the safety and low cost of ultrasound and the opportunity for fast and repeated molecular image acquisition. In order to extend the applicability of ultrasound molecular imaging, we have investigated rapid acquisition and the extension to 3D acquisition. We have demonstrated that ultrasound molecular imaging techniques can produce a high tumor-to-tissue ratio image within 2 minutes after injection, facilitating future application in interventional guidance. Further, the TLRH strategy applied here requires only a single transmitted pulse in each location at each timepoint and thus facilitates 3D imaging by speeding acquisition by a factor of three as compared with the three-pulse CPS imaging strategy.

The performance advantages of TLRH imaging are obtained without a sacrifice in signal to noise ratio or resolution, as compared with the widely used CPS technique. In an *in vitro* study, we verified that the axial resolution of T2R15 imaging was 2-fold higher than 2 MHz CPS imaging due to the higher resolution on receive. At a transmitted peak negative pressure of 250 kPa, reception at 15 MHz yielded a higher peak voltage than CPS, suggesting that T2R15 may be more sensitive than CPS, since the 15 MHz and 2.25 MHz transducers used in this study had very similar efficiency.

We found that acquisition of TLRH data at two minutes after microbubble injection (coupled with interframe filtering) resulted in high tumor-to-tissue background images. The half-life of the circulating agent is similarly on the order of a few minutes, and microbubbles appeared to accumulate in all points within the plane of interest (that were ultimately enhanced) within the two-minute interval. The adhesion of circulating microbubbles is expected to increase with time; however, it is reasonable to expect that microbubble detachment and fragmentation also increase with time [38, 39]. Using RF

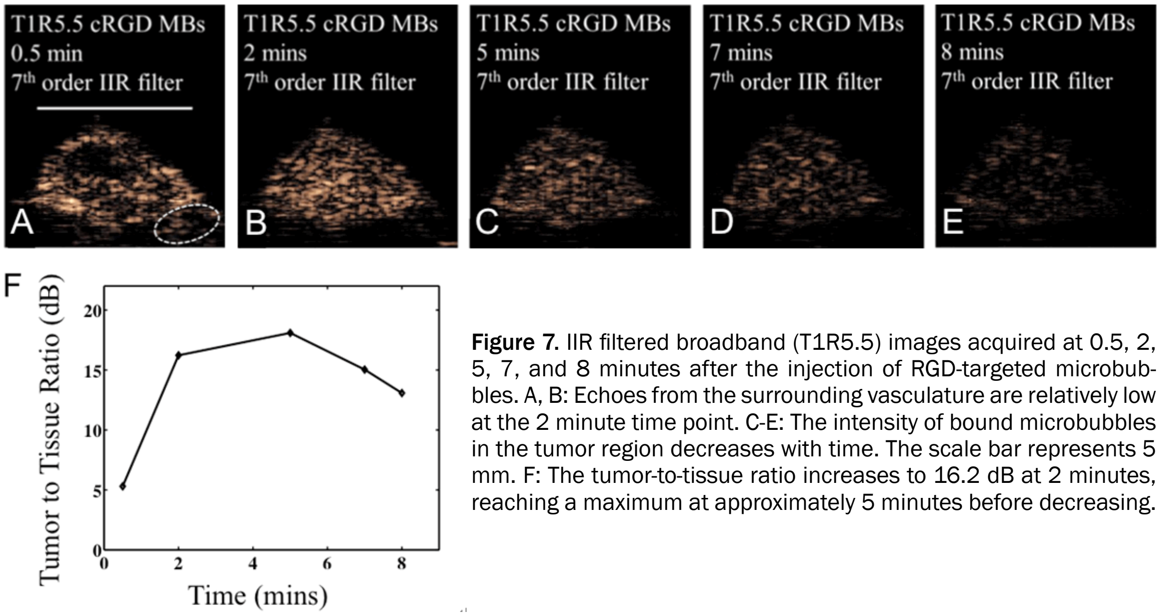

Figure 7. IIR filtered broadband (T1R5.5) images acquired at 0.5, 2, 5, 7, and 8 minutes after the injection of RGD-targeted microbubbles. A, B: Echoes from the surrounding vasculature are relatively low at the 2 minute time point. C-E: The intensity of bound microbubbles in the tumor region decreases with time. The scale bar represents 5 mm. F: The tumor-to-tissue ratio increases to 16.2 dB at 2 minutes, reaching a maximum at approximately 5 minutes before decreasing.

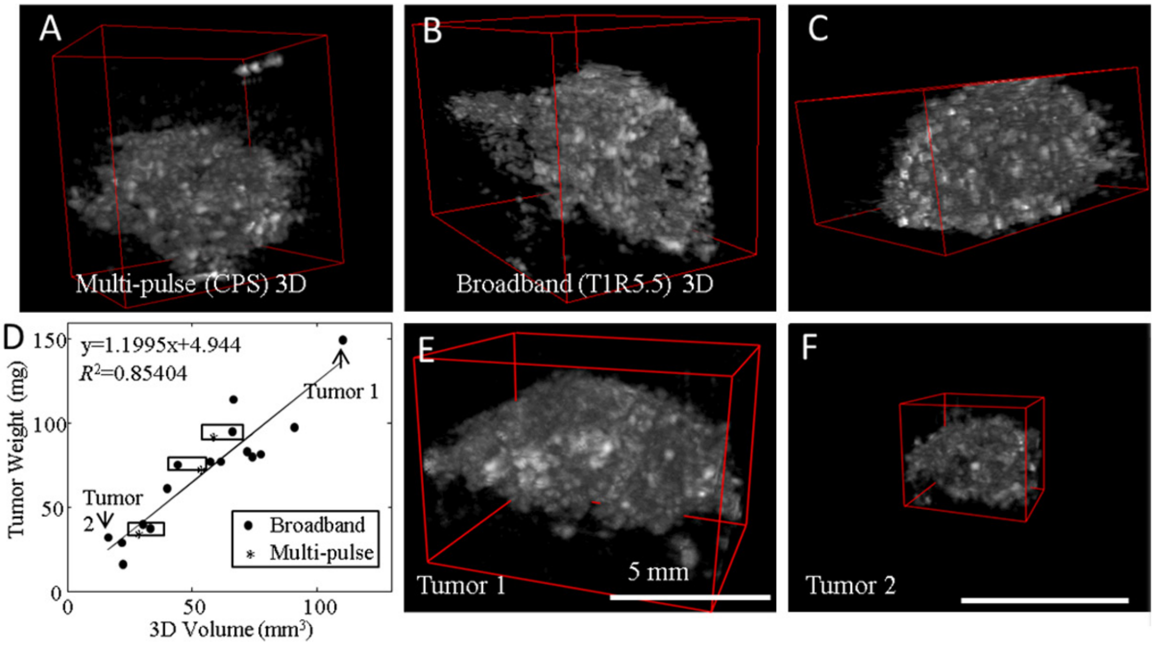

Figure 8. 3D visualization of targeted microbubbles using broadband and multi-pulse contrast imaging. A: 3D visualization of multi-pulse (CPS) images of bound microbubbles. B, C: 3D visualization of broadband (T1R5.5) images of bound microbubbles. Broadband (T1R5.5) volume image and CPS volume image depict the distribution of bound microbubbles, therefore indirectly displaying the distribution of $\alpha_v\beta_3$ integrin expression in the tumor region. E, F: Two representative 3D images show the maximum and the minimum volume measured in this study.

data acquired 2 minutes after microbubble injection, interframe filters are capable of suppressing the circulating microbubble echoes while retaining bound microbubble echoes (**Figures 4**, **5**). In the *in vivo* study, TLRH imaging with interframe filtering demonstrated efficient suppression (26.2±2.1 dB) of circulating microbubble echoes. The application of the interframe filter slightly reduced the mean intensity (3.7±1.2 dB) in the tumor region due to the suppression of circulating microbubble echoes in this region. Efficient separation of bound and circulating microbubble echoes requires filtering of uncompressed RF data that contains both amplitude and phase information. The interframe filter was substantially more efficient when applied to RF, as compared with video (detected) data, and the application of interframe filtering on video data could not effectively eliminate echoes from a high concentration of flowing microbubbles (**Figure 4F**) [21].

For the FIR interframe filter, the 30th order filter yielded the best rejection of moving microbubbles, but requires many RF data frames, which may not be desirable for visualizing bound microbubbles in a moving target tissue such as the heart. Since the tumor model used in this study was located in the lower abdomen of a mouse, the 3-second acquisition time required for an averaging filter was acceptable. A 7th order IIR filter achieves a similar performance as the 30th order FIR filter and requires fewer image frames (7 frames of RF data). The interframe filtering technique can be potentially combined with other high-resolution, high-sensitivity ultrasound contrast imaging techniques.

The morphological features in the distribution of bound microbubbles in the tumor region were consistent in both imaging modes. TLRH molecular imaging of non-targeted microbubbles showed significantly less contrast intensity in tumor regions, validating the specificity of the proposed imaging method. In addition, bound microbubble echoes were visualized on both the interframe filtered TLRH image (acquired at 2 minutes after the injection) and the non-filtered TLRH image (acquired after 7 minutes when most freely circulating microbubbles clear from the blood stream). TLRH images acquired at 7 minutes had a 3.5±0.8 dB reduction in intensity compared to TLRH images acquired at 2 minutes that may be due to the fragmentation and detachment of bound microbubbles.

The bound microbubbles visualized in 3D were primarily located in the tumor region, which further verified the specificity of the proposed imaging method. The tumor volume measured in the 3D image of bound microbubbles was correlated with the tumor weight; however, the estimated tumor volume is slightly lower than that estimated by weight. Here, the 3D image volume was estimated by fitting elliptical regions of interest in each plane; however, the molecular images are not accurately represented by smooth contours. Further, necrotic regions and challenges in excising the tumor tissue without including small regions of surrounding stroma may account for this difference. Taking advantage of the 3D visualization of targeted microbubbles, treatment planning and monitoring can be performed based on receptor characteristics, allowing for improved treatment planning. The 3D visualization of bound microbubbles could also potentially guide biopsy in larger animals.

Some limitations could be addressed to improve ultrasound molecular imaging. First, targeting microbubbles with a narrow or uniform size distribution could produce more uniform echoes [40, 41]. Thus, a linear relationship between the bound microbubble number and the received echo amplitude could be established, permitting a more accurate estimation of the concentration of targeting receptors. Second, the application of radiation force to manipulate targeted microbubbles towards the vascular endothelial cells could further reduce the time-interval between the microbubble injection and the data acquisition [42]. However, the potential of non-specific binding of targeted microbubbles must be carefully addressed in further *in vivo* work. Third, hardware delays in image acquisition limited the resolution in the scanning direction. An improved 3D scanning system and corresponding data acquisition strategies are currently under development. An alternative approach is to use a 2D imaging array for real-time 3D (4D) imaging. Fourth, the *in vivo* comparison between TLRH and CPS molecular imaging should be conducted in the same ultrasound imaging system. However, in this study, CPS molecular imaging on the Sequoia system was compared with TLRH on the Antares, due to the high quality CPS imaging that is available on the Sequoia and the multi-frequency imaging probes available on the Antares.

Conclusion

To conclude, using TLRH imaging and interframe filtering, we established a fast ultrasound molecular imaging method to visualize cRGD microbubble accumulation in a murine breast tumor model and successfully reduced the image acquisition time from 7 minutes to 2 minutes. The 3D visualization of bound microbubbles correctly delineates the tumor region, thus providing an accurate method to guide therapeutics.

Acknowledgements

The authors thank Azadeh Kheirolomoom, Eric Paoli and Douglas N. Stephens for assistance and valuable discussion, Julien Bec for help with 3D scanning system design, and Sarah M. Johnson for assistance with the *in vivo* studies. This work is supported by NIHR01CA112356, NIHR01CA103828, and NIHR01CA134659.

Address correspondence to: Katherine Ferrara, Department of Biomedical Engineering, University of California, Davis, 451 E Health Sciences Dr, Davis, CA 95616. Phone: 530-754-9436; Fax: 530-754-5739; E-mail: kwferrara@ucdavis.edu

References

[1] Ferrara K, Pollard R and Borden M. Ultrasound microbubble contrast agents: fundamentals and application to gene and drug delivery. Annu Rev Biomed Eng 2007; 9: 415-447.

[2] Qin S, Caskey CF and Ferrara KW. Ultrasound contrast microbubbles in imaging and therapy: physical principles and engineering. Phys Med Biol 2009; 54: R27-57.

[3] Cheung K, Couture O, Bevan PD, Cherin E, Williams R, Burns PN and Foster FS. In vitro characterization of the subharmonic ultrasound signal from Definity microbubbles at high frequencies. Phys Med Biol 2008; 53: 1209-1223.

[4] Bouakaz A, Frigstad S, Ten Cate FJ and de Jong N. Super harmonic imaging: a new imaging technique for improved contrast detection. Ultrasound Med Biol 2002; 28: 59-68.

[5] Simpson DH, Chin CT and Burns PN. Pulse Inversion Doppler: A New Method for Detecting Nonlinear Echoes from Microbubble Contrast Agents. IEEE Trans Ultrason Ferroelectr Freq Control 1999; 46: 372.

[6] Phillips P and Gardner E. Contrast-agent detection and quantification. Eur Radiol 2004; 14 Suppl 8: P4-10.

[7] Bleuzen A and Tranquart F. Incidental liver lesions: diagnostic value of cadence contrast pulse sequencing (CPS) and SonoVue. Eur Radiol 2004; 14 Suppl 8: P53-62.

[8] Albrecht T, Oldenburg A, Hohmann J, Skrok J, Hoffmann CW, Schettler S and Wolf KJ. Imaging of liver metastases with contrast-specific low-MI real-time ultrasound and SonoVue. Eur Radiol 2003; 13 Suppl 3: N79-86.

[9] Kruse DE and Ferrara KW. A new imaging strategy using wideband transient response of ultrasound contrast agents. IEEE Trans Ultrason Ferroelectr Freq Control 2005; 52: 1320-1329.

[10] Hu X, Zheng H, Kruse DE, Sutcliffe P, Stephens DN and Ferrara KW. A sensitive TLRH targeted imaging technique for ultrasonic molecular imaging. IEEE Trans Ultrason Ferroelectr Freq Control 2010; 57: 305-316.

[11] Gessner R, Lukacs M, Lee M, Cherin E, Foster FS and Dayton PA. High-resolution, high-contrast ultrasound imaging using a prototype dual-frequency transducer: in vitro and in vivo studies. IEEE Trans Ultrason Ferroelectr Freq Control 2010; 57: 1772-1781.

[12] Klibanov AL. Ligand-carrying gas-filled microbubbles: ultrasound contrast agents for targeted molecular imaging. Bioconjug Chem 2005; 16: 9-17.

[13] Kaufmann BA, Lewis C, Xie A, Mirza-Mohd A and Lindner JR. Detection of recent myocardial ischaemia by molecular imaging of P-selectin with targeted contrast echocardiography. Eur Heart J 2007; 28: 2011-2017.

[14] Weller GE, Lu E, Csikari MM, Klibanov AL, Fischer D, Wagner WR and Villanueva FS. Ultrasound imaging of acute cardiac transplant rejection with microbubbles targeted to intercellular adhesion molecule-1. Circulation 2003; 108: 218-224.

[15] Deshpande N, Ren Y, Foygel K, Rosenberg J and Willmann JK. Tumor angiogenic marker expression levels during tumor growth: longitudinal assessment with molecularly targeted microbubbles and US imaging. Radiology 2011; 258: 804-811.

[16] Willmann JK, Lutz AM, Paulmurugan R, Patel MR, Chu P, Rosenberg J and Gambhir SS. Dual-targeted contrast agent for US assessment of tumor angiogenesis in vivo. Radiology 2008; 248: 936-944.

[17] Lyshchik A, Fleischer AC, Huamani J, Hallahan DE, Brissova M and Gore JC. Molecular imaging of vascular endothelial growth factor receptor 2 expression using targeted contrast-enhanced high-frequency ultrasonography. J Ultrasound Med 2007; 26: 1575-1586.

[18] Pochon S, Tardy I, Bussat P, Bettinger T, Brochot J, von Wronski M, Passantino L and Schneider M. BR55: a lipopeptide-based VEGFR2-targeted ultrasound contrast agent for molecular imaging of angiogenesis. Invest Radiol 2010; 45: 89-95.

[19] Pysz MA, Foygel K, Rosenberg J, Gambhir SS, Schneider M and Willmann JK. Antiangiogenic cancer therapy: monitoring with molecular US

and a clinically translatable contrast agent (BR55). Radiology 2010; 256: 519-527.

[20] Tardy I, Pochon S, Theraulaz M, Emmel P, Passantino L, Tranquart F and Schneider M. Ultrasound molecular imaging of VEGFR2 in a rat prostate tumor model using BR55. Invest Radiol 2010; 45: 573-578.

[21] Anderson CR, Hu X, Zhang H, Tlaxca J, Decleves AE, Houghtaling R, Sharma K, Lawrence M, Ferrara KW and Rychak JJ. Ultrasound molecular imaging of tumor angiogenesis with an integrin targeted microbubble contrast agent. Invest Radiol 2011; 46: 215-224.

[22] Willmann JK, Kimura RH, Deshpande N, Lutz AM, Cochran JR and Gambhir SS. Targeted contrast-enhanced ultrasound imaging of tumor angiogenesis with contrast microbubbles conjugated to integrin-binding knottin peptides. J Nucl Med 2010; 51: 433-440.

[23] Desgrosellier JS and Cheresh DA. Integrins in cancer: biological implications and therapeutic opportunities. Nat Rev Cancer 2010; 10: 9-22.

[24] Lindner JR, Dayton PA, Coggins MP, Ley K, Song J, Ferrara K and Kaul S. Noninvasive imaging of inflammation by ultrasound detection of phagocytosed microbubbles. Circulation 2000; 102: 531-538.

[25] Jun HY, Park SH, Kim HS and Yoon KH. Long residence time of ultrasound microbubbles targeted to integrin in murine tumor model. Acad Radiol 2010; 17: 54-60.

[26] Anderson CR, Rychak JJ, Backer M, Backer J, Ley K and Klibanov AL. scVEGF microbubble ultrasound contrast agents: a novel probe for ultrasound molecular imaging of tumor angiogenesis. Invest Radiol 2010; 45: 579-585.

[27] Kaufmann BA, Carr CL, Belcik JT, Xie A, Yue Q, Chadderdon S, Caplan ES, Khangura J, Bullens S, Bunting S and Lindner JR. Molecular imaging of the initial inflammatory response in atherosclerosis: implications for early detection of disease. Arterioscler Thromb Vasc Biol 2010; 30: 54-59.

[28] Lee DJ, Lyshchik A, Huamani J, Hallahan DE and Fleischer AC. Relationship between retention of a vascular endothelial growth factor receptor 2 (VEGFR2)-targeted ultrasonographic contrast agent and the level of VEGFR2 expression in an in vivo breast cancer model. J Ultrasound Med 2008; 27: 855-866.

[29] Willmann JK, Paulmurugan R, Chen K, Gheysens O, Rodriguez-Porcel M, Lutz AM, Chen IY, Chen X and Gambhir SS. US imaging of tumor angiogenesis with microbubbles targeted to vascular endothelial growth factor receptor type 2 in mice. Radiology 2008; 246: 508-518.

[30] Weller GE, Wong MK, Modzelewski RA, Lu E, Klibanov AL, Wagner WR and Villanueva FS. Ultrasonic imaging of tumor angiogenesis using contrast microbubbles targeted via the tumor-binding peptide arginine-arginine-leucine. Cancer Res 2005; 65: 533-539.

[31] Needles A, Couture O and Foster FS. A method for differentiating targeted microbubbles in real time using subharmonic micro-ultrasound and interframe filtering. Ultrasound Med Biol 2009; 35: 1564-1573.

[32] Borden MA, Kruse DE, Caskey CF, Zhao S, Dayton PA and Ferrara KW. Influence of lipid shell physicochemical properties on ultrasound-induced microbubble destruction. IEEE Trans Ultrason Ferroelectr Freq Control 2005; 52: 1992-2002.

[33] Thomas L, Maslak S, Philips P and Holley G. Medical diagnostic ultrasound system using contrast pulse sequence imaging. United States Patent 2002.

[34] Borowsky AD, Namba R, Young LJ, Hunter KW, Hodgson JG, Tepper CG, McGoldrick ET, Muller WJ, Cardiff RD and Gregg JP. Syngeneic mouse mammary carcinoma cell lines: two closely related cell lines with divergent metastatic behavior. Clin Exp Metastasis 2005; 22: 47-59.

[35] Stephens DN, Kruse DE, Ergun AS, Barnes S, Lu XM and Ferrara KW. Efficient array design for sonotherapy. Phys Med Biol 2008; 53: 3943-3969.

[36] Caskey CF, Hlawitschka M, Qin S, Mahakian LM, Cardiff RD, Boone JM and Ferrara KW. An open environment CT-US fusion for tissue segmentation during interventional guidance. PLoS One 2011; 6: e27372.

[37] Prager RW, Rohling RN, Gee AH and Berman L. Rapid calibration for 3-D freehand ultrasound. Ultrasound Med Biol 1998; 24: 855-869.

[38] Takalkar AM, Klibanov AL, Rychak JJ, Lindner JR and Ley K. Binding and detachment dynamics of microbubbles targeted to P-selectin under controlled shear flow. J Control Release 2004; 96: 473-482.

[39] Dayton PA and Rychak JJ. Molecular ultrasound imaging using microbubble contrast agents. Front Biosci 2007; 12: 5124-42.

[40] Hettiarachchi K, Talu E, Longo ML, Dayton PA and Lee AP. On-chip generation of microbubbles as a practical technology for manufacturing contrast agents for ultrasonic imaging. Lab Chip 2007; 7: 463-468.

[41] Streeter JE, Gessner R, Miles I and Dayton PA. Improving sensitivity in ultrasound molecular imaging by tailoring contrast agent size distribution: in vivo studies. Mol Imaging 2010; 9: 87-95.

[42] Rychak JJ, Klibanov AL and Hossack JA. Acoustic radiation force enhances targeted delivery of ultrasound contrast microbubbles: in vitro verification. IEEE Trans Ultrason Ferroelectr Freq Control 2005; 52: 421-433.